energies

MDPI

*Article*

# Adaptive Current Control for Grid-Connected Inverter with Dynamic Recurrent Fuzzy-Neural-Network

**Yeqin Wang [1], Yan Yang [1,*], Rui Liang [1,2], Tao Geng [1] and Weixing Zhang [1]**

1 School of Automation, Huaiyin Institute of Technology, Huaian 223003, China; wangyeqin@hyit.edu.cn (Y.W.); liangrui@cumt.edu.cn (R.L.); hygxy13210@163.com (T.G.); zwx2068488186@163.com (W.Z.)
2 School of Electrical Engineering, China University of Mining and Technology, Xuzhou 221008, China
* Correspondence: yangyan@hyit.edu.cn; Tel.: +86-181-6875-6560

**Abstract:** The grid-connected inverter is a vital power electronic equipment connecting distributed generation (DG) systems to the utility grid. The quality of the grid-connected current is directly related to the safe and stable operation of the grid-connected system. This study successfully constructed a robust control system for a grid-connected inverter through a dynamic recurrent fuzzy-neural-network imitating sliding-mode control (DRFNNISMC) framework. Firstly, the dynamic model considering system uncertainties of the grid-connected inverter is described for the global integral sliding-mode control (GISMC) design. In order to overcome the chattering phenomena and the dependence of the dynamic information in the GISMC, a model-free dynamic recurrent fuzzy-neural-network (DRFNN) is proposed as a major controller to approximate the GISMC law without the extra compensator. In the DRFNN, a Petri net with varied threshold is incorporated to fire the rules, and only the parameters of the fired rules are adapted to alleviate the computational workload. Moreover, the network is designed with internal recurrent loops to improve the dynamic mapping capability considering the uncertainties in the control system. In addition, to assure the parameter convergence in the adaptation and the stability of the designed control system, the adaptation laws for the parameters of the DRFNN are deduced by the projection theorem and Lyapunov stability theory. Finally, the experimental comparisons with the GISMC scheme are performed in an inverter prototype to verify the superior performance of the proposed DRFNNISMC framework for the grid-connected current control.

**Keywords:** grid-connected inverter; global integral sliding-mode control (GISMC); dynamic recurrent fuzzy neural network (DRFNN); Petri net; robustness control



**Citation:** Wang, Y.; Yang, Y.; Liang, R.; Geng, T.; Zhang, W. Adaptive Current Control for Grid-Connected Inverter with Dynamic Recurrent Fuzzy-Neural-Network. *Energies* **2022**, *15*, 4163. https://doi.org/10.3390/en15114163

Academic Editor: Federico Barrero

Received: 6 May 2022
Accepted: 4 June 2022
Published: 6 June 2022



## 1. Introduction

Developing a new generation system based on distributed sources is a crucial way to achieve low carbon emissions and solve the problem of energy shortage. Microgrids (MGs) can significantly contribute to the utilization of distributed energy sources flexibly and efficiently and promote the transition from traditional grids to intelligent grids [1–4]. The electrical energy characteristic of the distributed power generation is different, and the output voltage easily fluctuates with changes of the environment. Therefore, grid-connected inverters are necessary interface units for distributed sources connecting to a MG or utility grid (UG) [5–7]. Research on advanced control strategies for inverter systems to enhance control capability is of great significance to promote the conversion efficiency of distributed sources, increase grid-connected capacity, and ensure the reliable operation of microgrids.

With the increase of nonlinear electric loads [8] and renewable energy systems [9] connected to the UG, the traditional linear control methods cannot guarantee the quality of the grid-connected current in the grid-connected inverter system with the existence of system uncertainties including DC voltage fluctuation, disturbance from the utility grid system, and variation of the circuit parameters. In recent years, as an effective nonlinear robust control scheme, sliding-mode control (SMC) [10] has attracted much attention in current control for inverters in grid-connected power-supply modes to replace the conventional linear control method. In sliding mode, SMCs can provide dynamic characteristics that are invariant to system uncertainties [11], so they can achieve good dynamic response and robustness under the occurrence of system uncertainties and disturbance. They are especially suitable for the control of power electronic circuits. However, the system dynamic loses insensitivity to uncertainties in the reaching phase. Fortunately, global sliding mode control (GSMC) can ensure the entire state trajectory of the controlled system in the sliding motion, and global robustness against system uncertainties can be obtained throughout the whole control process [12]. However, detailed system information is required in the SMC and the GSMC law. Moreover, it is hard to know detailed information of the system uncertainty in the practical grid-connected inverter system for the switching term in the control laws. Generally, a large gain is selected to cover uncertainties that inevitably cause chatting phenomena. Adaptive observers [13–15] are developed to approximate the uncertainty bound, thereby relieving the chattering phenomena, but the observation accuracy depends on the exact dynamic information of the controlled object.

Due to their ability to approximate an arbitrarily smooth function and independence from prior knowledge of the system model, intelligent control techniques (i.e., fuzzy logic, neural networks, and fuzzy neural networks) have [16–18] been an effective approach to constructing intelligent observers. Unfortunately, intelligent observers work as auxiliary controllers to estimate the unknown nonlinear part or uncertainties in the mathematical model. Moreover, an extra compensator is required for the approximation error, which increases the complexity of the controller design [19,20]. In order to solve the above problems, conventional nonlinear control strategies are integrated into the FNN to construct model-free intelligent control frameworks [21–24]. However, the feedforward network structure of the FNN causes a static problem in dealing with the dynamic system [25]. Although the adaptation of the weights and the membership function for the FNN can effectively enhance the dynamic ability, the feedforward FNN does not fully utilize the dynamic information within the network [22]. The recurrent FNN (RFNN) involves internal feedback loops to realize dynamic mapping, which can significantly ensure the dynamic performance and demonstrates more robust performance against unpredictable uncertainties [26–29]. High computational burden is a significant drawback of control systems based on FNN. In the conventional FNN, all parameters of the network are adjusted online. However, some rules can be redundant in the steady-state, and the adaptation of parameters corresponding to those rules will cause an unnecessary computational burden. The computational load can be reduced by involving a Petri net (PN) in the traditional FNN [30]. Therefore, this study aims to combine the Petri FNN and the RFNN to construct a dynamic recurrent FNN (DRFNN) for the current control of the grid-connected inverter, to preserve the superior dynamic and robust performance with less computational burden.

The main objective of this study is to construct a dynamic recurrent fuzzy-neural-network imitating sliding-mode control (DRFNNISMC) framework for a grid-connected inverter. The main contributions are as below:

(1) A DRFNN framework independent of the system dynamics is proposed as a major controller to approximate the designed global integral sliding-mode control (GISMC) law without the extra compensator. The proposed DRFNNISMC framework can effectively address the chattering phenomena in the model-based GISMC scheme in the presence of system uncertainties. The DRFNNISMC system proposed in this study has massive application potential in grid-connected inverter systems to deal with the system DC bus voltage and parameter variations, power disturbances, and nonlinear dynamics.

(2) The proposed DRFNN involves a Petri net with varied threshold and internal feedback loops to alleviate the computational burden and improve the dynamic mapping ability of the network. Therefore, the robustness to the uncertainties in the grid-connected inverter system is significantly enhanced by the proposed DRFNNISMC strategy.

(3) Although system stability and convergence of the network parameters are obtained in [31,32] according to the designed adaptation laws by the Lyapunov stability theorem, the possibility would exist that the update values of network parameters are out of the range of the boundaries. In order to avoid the singularity problem in the parameter adaptive process, the projection algorithm is also utilized to derive the adaptive laws for the network parameters.

Following the introduction, the circuit structure of the grid-connected inverter and the dynamic model considering system uncertainties will be depicted in Section 2. The model-based GIMSC scheme will be expressed in detail in Section 3. Then, the network structure and the adaptation laws for network parameters in DRFNN are investigated in Section 4. Section 5 will demonstrate the superiority of the proposed DRFNNISMC strategy by experimental results in a prototype of the inverter in grid-connected mode. Finally, in Section 6, some conclusions of this study will be drawn.

## 2. Descriptions of Grid-Connected Inverter

The framework of the grid-connected inverter is shown in Figure 1, which includes a full-bridge circuit and an $L$-type low-pass filter ($L_f$) with the equivalent resistors ($R_{Lf}$). The direct current (DC) bus input voltage and the alternating current (AC) output voltage are denoted as $V_{dc}$ and $v_{AB}$, respectively. $v_{Lf}$ represents the voltage across the filter. The single-phase full-bridge inverter works as a current source with the grid-connected current ($i_g$) and access to the utility grid ($v_g$). Meanwhile, the unpredictable disturbance in the utility grid system is considered as a voltage source ($v_{ld}$).

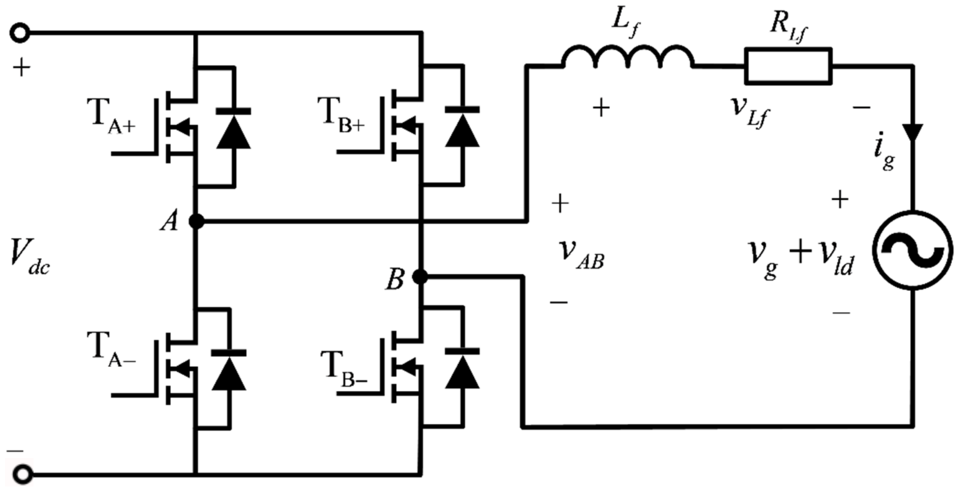


**Figure 1.** Framework of grid-connected inverter.

Applying the Kirchhoff voltage law (KVL) in the output loop of the grid-connected inverter in Figure 1 (generally, the equivalent resistor of the filter inductor is negligible), it can be derived as

$$\dot{i}_g = \frac{K_{\mathrm{PWM}}}{L_f} v_u - \frac{1}{L_f} v_g - \frac{1}{L_f} v_{ld}, \tag{1}$$

where $K_{\mathrm{PWM}}$ denotes the gain of the inverter by the unipolar PWM strategy. Generally, the filter inductance $L_f$ is supposed to be an ideal constant. However, even high-quality commercial inductance has a 10% tolerance [33]. On the other hand, disturbance incurred by the utility power and DC bus voltage is also inevitable. Considering the parameter variation and the disturbance in the utility grid, as well as the unmodeled system dynamic, the mathematical model in Equation (1) can be re-expressed as

$$\begin{aligned}\dot{x}(t) &= b_p u(t) + d_p f(t) + g(t) \\ &= (b_{pn} + \Delta b_{pn})u(t) + (d_{pn} + \Delta d_{pn})f(t) + g(t) \ , \\ &= b_{pn}u(t) + d_{pn}f(t) + \boldsymbol{\varphi}(t)\end{aligned} \tag{2}$$

where $\boldsymbol{x}(t) = i_g$, $u(t) = v_u$, $f(t) = v_g$, $g(t) = -v_{ld}/L_f$, $b_p = K_{PWM}/L_f$, and $d_p = -1/L_f$. $b_{pn}$ and $d_{pn}$ denote the criterion values of $b_p$ and $d_p$, respectively. $\Delta b_{pn}$ and $\Delta d_{pn}$ represent the error between the actual and the criterion values. The system lumped uncertainty $\varphi(t)$ is defined as

$$\varphi(t) = \Delta b_{pn}u(t) + \Delta d_{pn}f(t) + g(t), \tag{3}$$

**Assumption 1.** *The defined system lumped uncertainty in Equation (3) is a bounded function; assume that the boundary value can be expressed as*

$$|\varphi(t)| < \rho, \tag{4}$$

*where* $|\cdot|$ *represents the absolute operator and* $\rho$ *is a positive constant.*

## 3. GISMC Design

A global integral sliding-mode control (GISMC) strategy is designed to obtain the control target of regulating the grid-connected current ($i_g$) to track a sinusoidal reference signal ($i_g^*$) with fast dynamic response and high robustness for a grid-connected inverter. Moreover, a phase-locked loop (PLL) is adopted to capture the 0 unit sinusoidal function in the current command.

Firstly, the baseline model control law can be designed as

$$u_b(t) = b_{pn}^{-1}[-d_{pn}f(t) + \dot{x}^* + K_i e_i], \tag{5}$$

where $e_i = i_g^* - i_g$.

Substituting Equation (5) into the nominal part of the system model $\dot{x}(t) = b_{pn}u(t) + d_{pn}f(t)$, the controlled nominal system dynamic is

$$\dot{e}_i + K_i e_i = 0, \tag{6}$$

It is worth noting that the appropriate controller parameter ($K_i$) can be designed to obtain the desired dynamic control performance for the nominal model. However, if system uncertainties exist, the control performance index (e.g., rise time, overshoot, and settling time) specified by Equation (6) cannot be ensured by the control law shown in Equation (5), which designed based on the nominal model. Moreover, the controlled system will even lose its stability. In order to guarantee the control performance under the system uncertainties, a global sliding mode controller is designed.

Firstly, define a global integral sliding surface as

$$s(t) = C(e_i) - C(e_{i0}) + K_i \int_0^t \frac{\partial C}{\partial e_i} e_i(t)dt, \tag{7}$$

where $C(e_i)$ is designed to satisfy $\partial C/\partial e_i = b_{pn}^{-1}$; $e_{i0}$ is the initial value of $e_i(t)$; $K_i$ is a designed positive constant. It can be seen that $s(0) = 0$ and

$$\dot{s}(t) = \frac{\partial C}{\partial e_i}\dot{e}_i + \frac{\partial C}{\partial e_i}K_i e_i = 0, \tag{8}$$

Thus, $s(t) = 0$ for all $t \geq 0$. $s(t) = 0$ holds when $t = 0$. Therefore, the designed global sliding surface shown in Equation (7) has global robustness against system uncertainties without the reaching phase.

**Theorem 1.** *If the global integral sliding-mode control (GISMC) law is designed as Equation (9) for the grid-connected inverter shown in Equation (2), the current tracking error* $e_i(t)$ *will converge to 0 with* $t \to \infty$ *and the stability of the designed GISMC system for the grid-connected inverter considering the system uncertainties will be guaranteed.*

$$u_1(t) = b_{pn}^{-1}[-d_{pn}f(t) + \dot{x}^* + K_i e_i + K_s \mathrm{sgn}(s(t))], \tag{9}$$

*where* $K_s$ *is the designed switching control gain.*

**Proof of Theorem 1.** The first Lyapunov function candidate is defined as $V_1 = s^2/2$ and its derivative can be obtained as

$$\begin{aligned} \dot{V}_1 &= s\dot{s} \\ &= s[-K_S \mathrm{sgn}(s) - \varphi], \\ &\le -(K_S - |\varphi|)|s| \end{aligned} \tag{10}$$

Equation (10) will be hold under the condition of $K_S > \rho$; the first Lyapunov function and its derivative meet $V_1 > 0$ and $\dot{V}_1 \le 0$, respectively. Therefore, it can be proven that the grid-connected inverter system is stable by the designed GISMC law shown in Equation (9) and the current tracking error is convergent despite the existence of the system-lumped uncertainty. □

It is worth noting that the selection of the gain of the switching control law ($K_S$) is significant to the control performance, which is limited by the bound of the system uncertainty $\rho$. However, it is difficult to capture an accurate value for the system lumped uncertainty (e.g., DC bus voltage and parameter variations, power disturbance, and the nonlinear dynamics) in the practical application of grid-connected inverter systems [11]. If a too large $K_S$ is selected, chattering phenomena will be inevitable and generate a negative impact on the power electronic device, even exciting unstable system dynamics [21]. On the other side, if the value of $K_S$ is too small, the inequality Equation (10) may not meet $\dot{V}_1 \le 0$, especially in the worst cases. This will cause the designed control system to be unstable. Therefore, careful selection of the control gain is required to avoid an increase in chattering due to the switching term in Equation (9).

In order to attack the above problems of the SMC system, a dynamic recurrent fuzzy-neural-network (DRFNN) to imitate the GISMC framework is proposed for a grid-connected inverter in this study, which can ensure the robust control performance without the requirement of the prior system dynamic and the additional compensator, despite the existence of system uncertainties. Figure 2 depicts the block diagram of the proposed dynamic recurrent fuzzy-neural-network imitating sliding-mode control (DRFNNISMC) framework. Different from the traditional FNN controller, the proposed DRFNNISMC strategy selects the designed global integral sliding surface shown in Equation (7) as the input variable, and also adopts it to fire the useful rules and adaptation of the network parameters in the proposed DRFNNISMC strategy. In the DRFNN, to alleviate the computation burden of the network, only the contributing rules are fired by a designed Petri layer. Moreover, the dynamic mapping ability of the fuzzy neural network (FNN) can be enhanced by incorporating internal recurrent loops. In addition, the network parameters are designed with the capability of self-learning to further enhance the dynamic performance and ensure system stability. Finally, the output of the DRFNN is used as the control input of the grid-connected inverter.

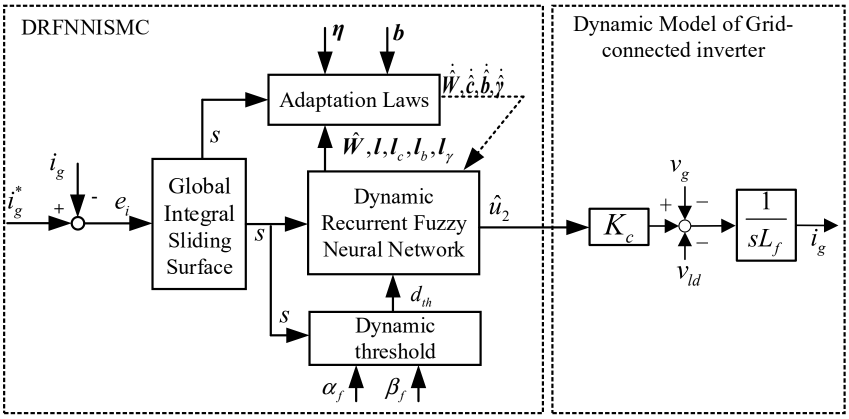


**Figure 2.** Block diagram of DRFNNISMC framework.

## 4. DRFNNISMC Design

### *4.1. Dynamic Recurrent Fuzzy-Neural-Network*

A DRFNNISMC scheme comprised of a five-layer fuzzy neural network (FNN) is shown in Figure 3. Internal feedback loops are incorporated into the membership layer and Petri nets are embedded between the rule and the output layer to construct the dynamic recurrent FNN (DRFNN) framework. The propagation of signals and the online learning laws for the proposed dynamic recurrent fuzzy-neural-network imitating sliding-mode control (DRFNNISMC) are described as follows.

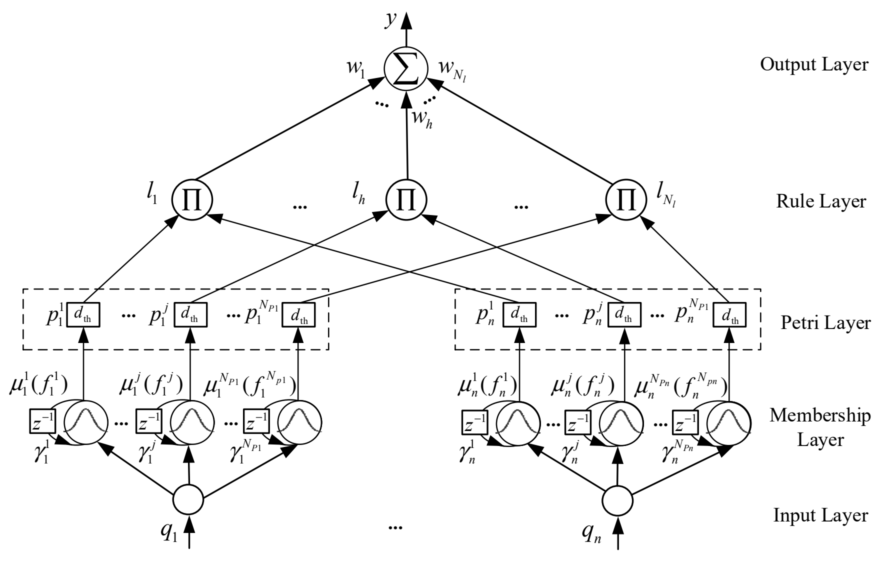


**Figure 3.** Framework of DRFNN.

#### 4.1.1. Input Layer

The input variables $q_i|_{i=1,\cdots,n}$ in this layer are delivered to the next layer directly.

#### 4.1.2. Gaussian Membership Layer with Recurrent Frame

The internal feedback loops for each node in this layer are introduced to construct recurrent framework. The inputs of the membership layer are represented as

$$f_i^j(n) = q_i(n) + \gamma_i^j \cdot \mu_i^j(n-1), \tag{11}$$

where $n$ represents the number of iterations; $\gamma_i^j$ denotes the recurrent weight; $\mu_i^j(n-1)$ indicates the output signal of the membership layer in the previous time. The Gaussian membership function is chosen for the membership layer that can be written as:

$$\mu_i^j(f_i^j) = \exp[-(f_i^j - c_i^j)^2/(b_i^j)^2]\Big|_{j=1,\cdots,N_{pi}}, \tag{12}$$

where $\exp[\cdot]$ is the exponential function; $c_i^j$ is the mean value, and $b_i^j$ is the standard deviation of the Gaussian function of the $j$th term for the $i$th input, respectively. The network parameters are collected into the vectors $\boldsymbol{c} = [c_1^1 \cdots c_1^{N_{p1}} \cdots c_n^1 \cdots c_n^{N_{pn}}]^T\Big|_{i=1,\cdots,n} \in \boldsymbol{R}^{N_r\times 1}$, $\boldsymbol{b} = [b_1^1 \cdots b_1^{N_{p1}} \cdots b_n^1 \cdots b_n^{N_{pn}}]^T\Big|_{i=1,\cdots,n} \in \boldsymbol{R}^{N_r\times 1}$, and $\boldsymbol{\gamma} = [\gamma_1^1 \cdots \gamma_1^{N_{p1}} \cdots \gamma_n^1 \cdots \gamma_n^{N_{pn}}]^T\Big|_{i=1,\cdots,n} \in \boldsymbol{R}^{N_r\times 1}$ in which $N_{pi}$ denotes the number of the Gaussian functions for the $i$th input and $N_r = \sum_{i=1}^{n} N_{p_i}$ denotes the total number of kernel functions of all input signals.

#### 4.1.3. Petri Layer

To improve the transient performance and the robustness of the FNN system, some membership functions are predetermined for the input signals by expert knowledge. However, the corresponding parameters of the redundant control rules are meaningless to update along with the decrease of the tracking error at the steady-state, which requires excessive computational resources. To solve the problem of the computation burden, a dynamic Petri net [25] is incorporated into the traditional FNN structure to only transfer the significant rules to the next layer. The competition law in the Petri layer for producing the tokens to fire useful rules is selected as:

$$p_i^j = \begin{cases} 1 & if\ \mu_i^j(f_i^j) \geq d_{\text{th}} \\ 0 & otherwise \end{cases}, \tag{13}$$

where $p_i^j$ is the transition of the neuron in the membership layer. If the outputs of the neuron in the membership layer are larger than the dynamic threshold value ($d_{\text{th}}$), the transition $p_i^j$ will be set as 1; otherwise, it will be set as 0. Then, only the neuron in the membership layer with token 1 will be fired and propagated to the next layer by the Petri net. Moreover, the dynamic threshold value ($d_{\text{th}}$) is tuned by the sliding-surface function ($s$), which is designed as

$$d_{\text{th}} = \frac{\alpha_f \exp[-\beta_f(\frac{1}{2}ss^T)]}{1+\exp[-\beta_f(\frac{1}{2}ss^T)]}, \tag{14}$$

where $\alpha_f$ and $\beta_f$ are positive constants. It can be seen that the threshold values will be decreased with a larger tracking error to activate more membership neurons and vice versa.

#### 4.1.4. Layer 4 Rule Layer

Each neuron in the rule layer multiplies the fired outputs of the membership layer according to different input signals. The result of the product for the $h$th rule can be presented as

$$l_h = \begin{cases} \prod_{i=1}^{n} \mu_i^j(f_i^j)\Big|_{h=1,\cdots,N_l}, & p_i^j = 1 \\ 0, & p_i^j = 0 \end{cases}, \tag{15}$$

where $N_l$ is the number of nodes in the rule layer. All the rules $l_h|_{h=1,\cdots,N_l}$ are gathered as a vector of $\boldsymbol{l} = [l_1 \cdots l_h \cdots l_{N_l}]^T \in R^{N_l\times 1}$.

4.1.5. Layer 5 Output Layer

This layer multiplies each rule with corresponding weights as the input of the output layer, and the summation of all the input signals is the output of the FNN. The output can be expressed in following form:

$$y = \sum_{h=1}^{N_l} w_h l_h = \boldsymbol{Wl}, \tag{16}$$

where $w_h$ is the connecting weight from the $h$th rule layer to the output layer. The weigh vector $\boldsymbol{W} = [w_1 \cdots w_h \cdots w_{N_l}] \in R^{1\times N_l}$ is defined for collecting the weighs.

*4.2. Adaptive Scheme for Parameters of DRFNN*

The approximation error between the GISMC law and the optimal DRNNISMC law is defined for the derivation of the adaptive laws of the network parameters. Moreover, the Lyapunov stability theory [34] and the projection theorem [35] are adopted to guarantee the parameter convergence in the self-adaptive process and the global stability of the designed DRNNISMC system.

The proposed DRNNISMC law can be represented as follows:

$$u_2(s, \boldsymbol{W}, \boldsymbol{c}, \boldsymbol{b}, \gamma) \equiv \boldsymbol{Wl}(s, \boldsymbol{c}, \boldsymbol{b}, \gamma), \tag{17}$$

**Assumption 2.** *There are optimal network parameters containing weight matrix ($\boldsymbol{W}^*$), mean vectors ($\boldsymbol{c}^*$), standard deviation vectors ($\boldsymbol{b}^*$), and recurrent weight ($\gamma^*$) for an optimal DRNNISMC law ($u_2^*$) to imitate the GISMC law in (6). The optimal DRNNISMC law is expressed as*

$$u_1 = u_2^*(s, \boldsymbol{W}^*, \boldsymbol{c}^*, \boldsymbol{b}^*, \gamma^*) = \boldsymbol{W}^*\boldsymbol{l}^*(\boldsymbol{s}, \boldsymbol{c}^*, \boldsymbol{b}^*, \gamma^*) + \varepsilon, \tag{18}$$

*where $\boldsymbol{W}^*$, $\boldsymbol{c}^*$, $\boldsymbol{b}^*$, $\gamma^*$, and $\boldsymbol{l}^*$ are the optimal vectors of $\boldsymbol{W}$, $\boldsymbol{c}$, $\boldsymbol{b}$, $\gamma$, and $\boldsymbol{l}$ respectively; $\varepsilon$ is the minimum mapping error vector.*

The estimation of the GISMC law by the DRNN can be presented as

$$\hat{\boldsymbol{u}}_2(s,\ \hat{\boldsymbol{W}},\ \hat{\boldsymbol{c}}\ , \hat{\boldsymbol{b}}, \hat{\gamma}) = \hat{\boldsymbol{W}}\hat{\boldsymbol{l}}(s,\ \hat{\boldsymbol{W}},\ \hat{\boldsymbol{c}}\ , \hat{\boldsymbol{b}}, \hat{\gamma}), \tag{19}$$

where $\hat{\boldsymbol{W}}$, $\hat{\boldsymbol{c}}$, $\hat{\boldsymbol{b}}$, $\hat{\gamma}$ and $\hat{\boldsymbol{l}}$ denote the estimated values of $\boldsymbol{W}^*$, $\boldsymbol{c}^*$, $\boldsymbol{b}^*$, $\gamma^*$, and $\boldsymbol{l}^*$, respectively. The approximation error ($\widetilde{u}$) between the estimation of the GISMC law ($u_1$) and the optimal DRNNISMC law ($u_2^*$) is defined as

$$\begin{aligned} \widetilde{u} &= u_2^* - \hat{u}_2 + \varepsilon \\ &= \boldsymbol{W}^*\boldsymbol{l}^*(s, \boldsymbol{c}^*, \boldsymbol{b}^*, \gamma^*) - \hat{\boldsymbol{W}}\hat{\boldsymbol{l}}(s,\ \hat{\boldsymbol{c}}, \hat{\boldsymbol{b}}, \hat{\gamma}) + \varepsilon\ ' \end{aligned} \tag{20}$$

In order to be convenient for later stability analyses, the Taylor series expansion is employed to transform the output of the rule layer ($\boldsymbol{l}$) into partially linear forms. The following linearization expansion for $\widetilde{\boldsymbol{l}}$ can be obtained

$$\widetilde{\boldsymbol{l}} = \left[\widetilde{l}_1\ \widetilde{l}_2 \cdots \widetilde{l}_{N_l}\right]^T \equiv \boldsymbol{l}_c\widetilde{\boldsymbol{c}} + \boldsymbol{l}_b\widetilde{\boldsymbol{b}} + \boldsymbol{l}_\gamma\widetilde{\gamma} + \boldsymbol{h}, \tag{21}$$

where $\boldsymbol{l}_c = \left[\frac{\partial \hat{l}_1}{\partial \hat{\boldsymbol{c}}}\ \frac{\partial \hat{l}_2}{\partial \hat{\boldsymbol{c}}} \cdots \frac{\partial \hat{l}_{N_l}}{\partial \hat{\boldsymbol{c}}}\right]^T|_{\hat{\boldsymbol{c}}=\boldsymbol{c}^*} \in R^{N_l\times N_r}$; $\boldsymbol{l}_b = \left[\frac{\partial \hat{l}_1}{\partial \hat{\boldsymbol{b}}}\ \frac{\partial \hat{l}_2}{\partial \hat{\boldsymbol{b}}} \cdots \frac{\partial \hat{l}_{N_l}}{\partial \hat{\boldsymbol{b}}}\right]^T|_{\hat{\boldsymbol{b}}=\boldsymbol{b}^*} \in R^{N_l\times N_r}$; $\boldsymbol{l}_\gamma = \left[\frac{\partial \hat{l}_1}{\partial \hat{\gamma}}\ \frac{\partial \hat{l}_2}{\partial \hat{\gamma}} \cdots \frac{\partial \hat{l}_{N_l}}{\partial \hat{\gamma}}\right]^T|_{\hat{\gamma}=\gamma^*} \in R^{N_l\times N_r}$; $\widetilde{\boldsymbol{l}} = \boldsymbol{l}^* - \hat{\boldsymbol{l}}$, $\widetilde{\boldsymbol{c}} = \boldsymbol{c}^* - \hat{\boldsymbol{c}}$, $\widetilde{\boldsymbol{b}} = \boldsymbol{b}^* - \hat{\boldsymbol{b}}$, and $\widetilde{\gamma} = \gamma^* - \hat{\gamma}$, respectively, and $\boldsymbol{h} \in R^{N_l\times 1}$ is the summation of the higher-order term in the Taylor series.

Then, the optimal value of rule ($\boldsymbol{l}$) can be rewritten as

$$\boldsymbol{l}^* = \hat{\boldsymbol{l}} + \widetilde{\boldsymbol{l}} = \hat{\boldsymbol{l}} + \boldsymbol{l}_c\widetilde{\boldsymbol{c}} + \boldsymbol{l}_b\widetilde{\boldsymbol{b}} + \boldsymbol{l}_\gamma\widetilde{\gamma} + \boldsymbol{h}, \tag{22}$$

Substitute (22) into the approximation error ($\widetilde{u}$) in Equation (21) to obtain

$$\begin{aligned}\widetilde{u} &= \boldsymbol{W}^{*}\boldsymbol{l}^{*} - \hat{\boldsymbol{W}}\hat{\boldsymbol{l}} + \varepsilon \\ &= \boldsymbol{W}^{*}(\hat{\boldsymbol{l}} + \boldsymbol{l}_c\widetilde{\boldsymbol{c}} + \boldsymbol{l}_b\widetilde{\boldsymbol{b}} + \boldsymbol{l}_\gamma\widetilde{\boldsymbol{\gamma}} + \boldsymbol{h}) - \hat{\boldsymbol{W}}\hat{\boldsymbol{l}} + \varepsilon \\ &= (\boldsymbol{W}^{*} - \hat{\boldsymbol{W}})\hat{\boldsymbol{l}} + (\hat{\boldsymbol{W}} + \widetilde{\boldsymbol{W}})\boldsymbol{l}_c\widetilde{\boldsymbol{c}} + (\hat{\boldsymbol{W}} + \widetilde{\boldsymbol{W}})\boldsymbol{l}_b\widetilde{\boldsymbol{b}} + (\hat{\boldsymbol{W}} + \widetilde{\boldsymbol{W}})\boldsymbol{l}_\gamma\widetilde{\boldsymbol{\gamma}} + \boldsymbol{W}^{*}\boldsymbol{h} + \varepsilon \\ &= \widetilde{\boldsymbol{W}}\hat{\boldsymbol{l}} + \hat{\boldsymbol{W}}\boldsymbol{l}_c\widetilde{\boldsymbol{c}} + \hat{\boldsymbol{W}}\boldsymbol{l}_b\widetilde{\boldsymbol{b}} + \hat{\boldsymbol{W}}\boldsymbol{l}_\gamma\widetilde{\boldsymbol{\gamma}} + \widetilde{\boldsymbol{W}}(\boldsymbol{l}_c\widetilde{\boldsymbol{c}} + \boldsymbol{l}_b\widetilde{\boldsymbol{b}} + \boldsymbol{l}_\gamma\widetilde{\boldsymbol{\gamma}}) + \boldsymbol{W}^{*}\boldsymbol{h} + \varepsilon \\ &= \widetilde{\boldsymbol{W}}\hat{\boldsymbol{l}} + \hat{\boldsymbol{W}}\boldsymbol{l}_c\widetilde{\boldsymbol{c}} + \hat{\boldsymbol{W}}\boldsymbol{l}_b\widetilde{\boldsymbol{b}} + \hat{\boldsymbol{W}}\boldsymbol{l}_\gamma\widetilde{\boldsymbol{\gamma}} + H\end{aligned}, \tag{23}$$

where $\widetilde{\boldsymbol{W}} = \boldsymbol{W}^{*} - \hat{\boldsymbol{W}}$ and $H = \widetilde{\boldsymbol{W}}(\boldsymbol{l}_c\widetilde{\boldsymbol{c}} + \boldsymbol{l}_b\widetilde{\boldsymbol{b}} + \boldsymbol{l}_\gamma\widetilde{\boldsymbol{\gamma}}) + \boldsymbol{W}^{*}\boldsymbol{h} + \varepsilon$ represents the uncertain term.

**Theorem 2.** *The dynamic model of the grid-connected inverter is modeled by Equation (2). If the proposed DRFNNISMC strategy is designed as described in Equation (17), the adaptation laws for the parameters in DRFNN are designed as depicted in Equations (24)–(31). Then, the current tracking error and the estimated errors ($\widetilde{\boldsymbol{W}}$, $\widetilde{\boldsymbol{c}}$, $\widetilde{\boldsymbol{b}}$ and $\widetilde{\boldsymbol{\gamma}}$ ) are stably convergent.*

$$\begin{aligned}&\text{If } (\|\hat{\boldsymbol{W}}\| < b_w) \text{ or } (\|\hat{\boldsymbol{W}}\| = b_w \text{ and } s\hat{\boldsymbol{W}}\hat{\boldsymbol{l}} \le 0) \\ &\dot{\hat{\boldsymbol{W}}}^T = \eta_w s\hat{\boldsymbol{l}}\end{aligned}, \tag{24}$$

$$\begin{aligned}&\text{If } (\|\hat{\boldsymbol{W}}\| = b_w \text{ and } s\hat{\boldsymbol{W}}\hat{\boldsymbol{l}} > 0) \\ &\dot{\hat{\boldsymbol{W}}}^T = \eta_w (s\hat{\boldsymbol{l}} - \tfrac{s\hat{\boldsymbol{l}}\hat{\boldsymbol{W}}\hat{\boldsymbol{W}}^T}{\|\hat{\boldsymbol{W}}\|^2})\end{aligned}, \tag{25}$$

$$\begin{aligned}&\text{If } (\|\hat{\boldsymbol{c}}\| < b_c) \text{ or } (\|\hat{\boldsymbol{c}}\| = b_c \text{ and } s\hat{\boldsymbol{W}}\boldsymbol{l}_c\hat{\boldsymbol{c}} \le 0) \\ &\dot{\hat{\boldsymbol{c}}}^T = \eta_c s\hat{\boldsymbol{W}}\boldsymbol{l}_c\end{aligned}, \tag{26}$$

$$\begin{aligned}&\text{If } (\|\hat{\boldsymbol{c}}\| = b_c \text{ and } s\hat{\boldsymbol{W}}\boldsymbol{l}_c\hat{\boldsymbol{c}} > 0) \\ &\dot{\hat{\boldsymbol{c}}}^T = \eta_c (s\hat{\boldsymbol{W}}\boldsymbol{l}_c - \tfrac{s\hat{\boldsymbol{W}}\boldsymbol{l}_c\hat{\boldsymbol{c}}\hat{\boldsymbol{c}}^T}{\|\hat{\boldsymbol{c}}\|^2})\end{aligned}, \tag{27}$$

$$\begin{aligned}&\text{If } (\|\hat{\boldsymbol{b}}\| < b_b) \text{ or } (\|\hat{\boldsymbol{b}}\| = b_b \text{ and } s\hat{\boldsymbol{W}}\boldsymbol{l}_b\hat{\boldsymbol{b}} \le 0) \\ &\dot{\hat{\boldsymbol{b}}}^T = \eta_b s\hat{\boldsymbol{W}}\boldsymbol{l}_b\end{aligned}, \tag{28}$$

$$\begin{aligned}&\text{If } (\|\hat{\boldsymbol{b}}\| = b_b \text{ and } s\hat{\boldsymbol{W}}\boldsymbol{l}_b\hat{\boldsymbol{b}} > 0) \\ &\dot{\hat{\boldsymbol{b}}}^T = \eta_c (s\hat{\boldsymbol{W}}\boldsymbol{l}_b - \tfrac{s\hat{\boldsymbol{W}}\boldsymbol{l}_b\hat{\boldsymbol{b}}\hat{\boldsymbol{b}}^T}{\|\hat{\boldsymbol{b}}\|^2})\end{aligned}, \tag{29}$$

$$\begin{aligned}&\text{If } (\|\hat{\boldsymbol{\gamma}}\| < b_\gamma) \text{ or } (\|\hat{\boldsymbol{\gamma}}\| = b_\gamma \text{ and } s\hat{\boldsymbol{W}}\boldsymbol{l}_\gamma\hat{\boldsymbol{\gamma}} \le 0) \\ &\dot{\hat{\boldsymbol{\gamma}}}^T = \eta_\gamma s\hat{\boldsymbol{W}}\boldsymbol{l}_\gamma\end{aligned}, \tag{30}$$

$$\begin{aligned}&\text{If } (\|\hat{\boldsymbol{\gamma}}\| = b_\gamma \text{ and } s\hat{\boldsymbol{W}}\boldsymbol{l}_\gamma\hat{\boldsymbol{\gamma}} > 0) \\ &\dot{\hat{\boldsymbol{\gamma}}}^T = \eta_\gamma (s\hat{\boldsymbol{W}}\boldsymbol{l}_\gamma - \tfrac{s\hat{\boldsymbol{W}}\boldsymbol{l}_\gamma\hat{\boldsymbol{\gamma}}\hat{\boldsymbol{\gamma}}^T}{\|\hat{\boldsymbol{\gamma}}\|^2})\end{aligned}, \tag{31}$$

*where $\|\cdot\|$ is the Euclidean norm operator; $b_w$, $b_c$, $b_b$, and $b_\gamma$ are bound values; $\eta_w$, $\eta_c$, $\eta_b$, and $\eta_\gamma$ are learning rates. The bounds values and learning rates are all given positive values. In Figure 3, $\boldsymbol{\eta} = [\eta_w\ \eta_c\ \eta_b\ \eta_\gamma]$ and $\boldsymbol{b} = [b_w\ b_c\ b_b\ b_\gamma]$ are defined as learning-rate vector and bound vector, respectively.*

*4.3. Stability Analysis of DRFNNISMC*

**Proof of Theorem 2.** The following second Lyapunov function is defined for the proposed DRFNNISMC system:

$$V_2(s, \widetilde{\boldsymbol{W}}, \widetilde{\boldsymbol{c}}, \widetilde{\boldsymbol{b}}) = \frac{1}{2}s^2 + \frac{\widetilde{\boldsymbol{W}}\widetilde{\boldsymbol{W}}^T}{2\eta_w} + \frac{\widetilde{\boldsymbol{c}}^T\widetilde{\boldsymbol{c}}}{2\eta_c} + \frac{\widetilde{\boldsymbol{b}}^T\widetilde{\boldsymbol{b}}}{2\eta_b} + \frac{\widetilde{\boldsymbol{\gamma}}^T\widetilde{\boldsymbol{\gamma}}}{2\eta_\gamma}, \tag{32}$$

By differentiating Equation (31), one can obtain

$$\begin{aligned}\dot{V}_2(s,\widetilde{\boldsymbol{W}},\widetilde{\boldsymbol{c}},\widetilde{\boldsymbol{b}},\widetilde{\gamma}) &= s\dot{s} - \frac{\widetilde{\boldsymbol{W}}\dot{\hat{\boldsymbol{W}}}^T}{\eta_w} - \frac{\dot{\hat{\boldsymbol{c}}}^T\widetilde{\boldsymbol{c}}}{\eta_c} - \frac{\dot{\hat{\boldsymbol{b}}}^T\widetilde{\boldsymbol{b}}}{\eta_b} - \frac{\dot{\hat{\gamma}}^T\widetilde{\gamma}}{\eta_\gamma} \\ &= s[-K_S\mathrm{sgn}(s) - \varphi + H] + V_w + V_c + V_b + V_\gamma \\ &\le -(K_S - |H-\varphi|)|s| \le 0\end{aligned}, \tag{33}$$

where $V_w = s\widetilde{\boldsymbol{W}}\hat{\boldsymbol{l}} - \frac{\widetilde{\boldsymbol{W}}\dot{\hat{\boldsymbol{W}}}^T}{\eta_w}$, $V_c = s\hat{\boldsymbol{W}}\boldsymbol{l_c}\widetilde{\boldsymbol{c}} - \frac{\dot{\hat{\boldsymbol{c}}}^T\widetilde{\boldsymbol{c}}}{\eta_c}$, $V_b = s\hat{\boldsymbol{W}}\boldsymbol{l_b}\widetilde{\boldsymbol{b}} - \frac{\dot{\hat{\boldsymbol{b}}}^T\widetilde{\boldsymbol{b}}}{\eta_b}$, and $V_\gamma = s\hat{\boldsymbol{W}}\boldsymbol{l}_\gamma\widetilde{\boldsymbol{\gamma}} - \frac{\dot{\hat{\gamma}}^T\widetilde{\gamma}}{\eta_\gamma}$. If the controller gain of $K_S > |H-\psi|$ is satisfied, the result of $\dot{V}_2(s,\widetilde{\boldsymbol{W}},\widetilde{\boldsymbol{c}},\widetilde{\boldsymbol{b}},\widetilde{\gamma}) \le 0$ can be achieved. The detailed deduction of Equation (33) is depicted in Appendix A. From Equation (33), since $\dot{V}_2(s,\widetilde{\boldsymbol{W}},\widetilde{\boldsymbol{c}},\widetilde{\boldsymbol{b}},\widetilde{\gamma})$ is negative semi-definite, i.e., $\dot{V}_2(s,\widetilde{\boldsymbol{W}},\widetilde{\boldsymbol{c}},\widetilde{\boldsymbol{b}},\widetilde{\gamma}) \le \dot{V}_2(s(0),\widetilde{\boldsymbol{W}},\widetilde{\boldsymbol{c}},\widetilde{\boldsymbol{b}},\widetilde{\gamma})$, then $s(t)$, $\widetilde{\boldsymbol{W}}$, $\widetilde{\boldsymbol{c}}$, $\widetilde{\boldsymbol{b}}$ and $\widetilde{\gamma}$ are bounded.

Define a function $G(t) \equiv (K_S - |H-\varphi|)|s| = -\dot{V}_2(s,\widetilde{\boldsymbol{W}},\widetilde{\boldsymbol{c}},\widetilde{\boldsymbol{b}},\widetilde{\gamma})$ and integrate $G(t)$ with respect to time to obtain

$$\int_0^t G(\tau)\,d\tau \le V_2(s(0),\widetilde{\boldsymbol{W}},\widetilde{\boldsymbol{c}},\widetilde{\boldsymbol{b}},\widetilde{\gamma}) - V_2(s(t),\widetilde{\boldsymbol{W}},\widetilde{\boldsymbol{c}},\widetilde{\boldsymbol{b}},\widetilde{\gamma}), \tag{34}$$

Since $V_2(s(0),\widetilde{\boldsymbol{W}},\widetilde{\boldsymbol{c}},\widetilde{\boldsymbol{b}},\widetilde{\gamma})$ is bounded and $V_2(s(t),\widetilde{\boldsymbol{W}},\widetilde{\boldsymbol{c}},\widetilde{\boldsymbol{b}},\widetilde{\gamma})$ is non-increasing and bounded, one can conclude that $\lim_{t\to\infty}\int_0^t G(\tau)\,d\tau < \infty$ and $\dot{G}(t)$ is bounded. According to Barbalat's Lemma [34], one can conclude that $s(t)$, $\widetilde{\boldsymbol{W}}$, $\widetilde{\boldsymbol{c}}$, $\widetilde{\boldsymbol{b}}$, and $\widetilde{\gamma}$ will converge to zero as $t \to \infty$. As a result, the proposed DRFNNISMC system is proven to be stable. Moreover, the adaptation laws can guarantee the convergence of the parameters in DRFNN. □

The execution process of the designed DRFNNISMC strategy is depicted in the flowchart shown in Figure 4.

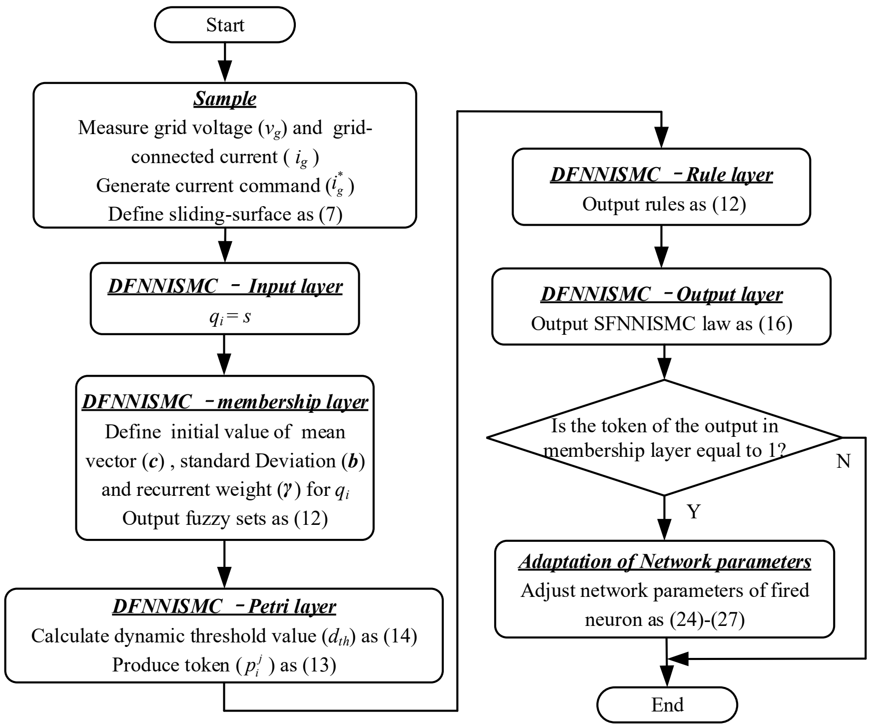


**Figure 4.** Flowchart for the execution process of the designed DRFNNISMC strategy.

## 5. Experimental Verification

The effectiveness of the proposed DRFNNISMC strategy is demonstrated in an experimental prototype shown in Figure 5 and the detailed circuit parameters of the grid-connected inverter are described in Table 1. Moreover, the grid-connected current and the utility voltage are measured by the Hall current and voltage sensor, respectively. In addition, a digital phase-locked-loop (PLL) is designed to supply a unit sinusoidal waveform that keeps in phase with the utility voltage for the current command. Furthermore, the proposed control algorithms and the digital PLL are realized in a digital signal processor (DSP) board (TMS320F28335) using "C" codes, and the pulse-width-modulation (PWM) signals are generated through ePWM modules. Then, the PWM signals are sent to the driving circuit to generate the control signal for the power switches (FQA24N50F power MOSFETs). Finally, a digital oscilloscope is used to display the waveforms of the grid voltage and the grid-connected current.

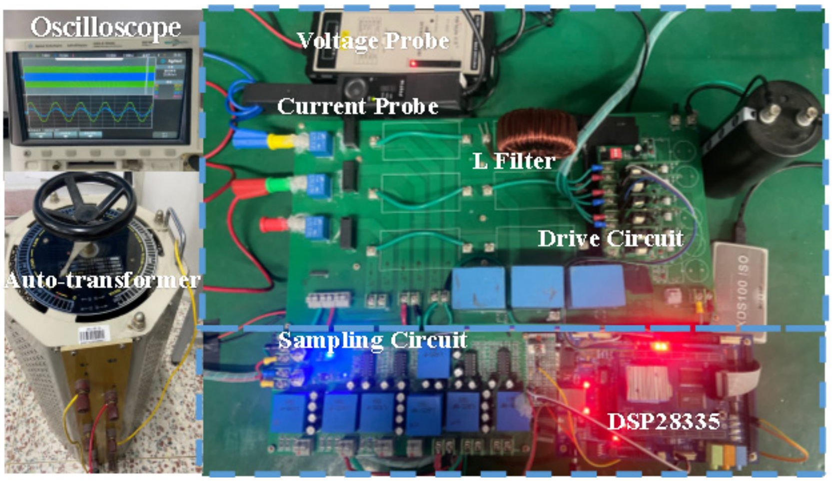


**Figure 5.** Experimental prototype of grid-connected inverter.

**Table 1.** Values of parameters for grid-connected inverter.

| Circuit Parameters | Value |
|---|---|
| DC bus voltage | 200 V |
| Current command (RMS) | 10 A |
| Grid voltage (RMS) | 110 V |
| Filter inductance | 2 mH |
| Fundamental frequency | 50 Hz |
| Switching frequency | 15 kHz |

In this study, the number of membership functions for the input node is designed as $N_{p1} = 3$, the initial mean values are set as $c_{i=1,\cdots,n;j=1,\cdots,N_{p1}} = 3 \times \left(j - \frac{N_p + 1}{2}\right)$, initial standard deviation values are selected as $b_i^j\Big|_{i=1,\cdots,n;j=1,\cdots,N_{pi}} = 3$, the initial weight of the self-feedback loop $\gamma_i^j\Big|_{i=1,\cdots,n;j=1,\cdots,N_{pi}} = 0.5$, and the initial weight ($\boldsymbol{W}$) is set as zero vector. The parameter values roughly initialized based on expert knowledge are adjusted online to the optimal values for satisfactory responses according to the adaptation laws in Equations (24)–(31). Moreover, the adaptive learning rates of the network parameters are selected as $\eta_w = 0.26$, $\eta_c = \eta_b = 8.55 \times 10^{-4}$, $\eta_\gamma = 0.12$. The parameters in the dynamic threshold value for the Petri layer are chosen as $\alpha_f = 0.15$, $\beta_f = 350$.

Comparative experiments on the global integral sliding-mode control (GISMC) and the proposed dynamic recurrent fuzzy-neural-network imitating sliding-mode control (DRFNNISMC) are performed in this study. The parameters of the GISMC and the proposed

DRFNNISMC are selected to achieve similar control performance with each other in the nominal case, and the control parameters for the global integral sliding surface used in GISMC and the proposed DRFNNISMC are both selected as $k_i = 1.45 \times 10^3$, $k_s = 0.86$ for a fair comparison. Furthermore, to record the respective control performances of the two control strategies, a normalized mean square error (NMSE) value of the current tracking error is expressed as

$$\mathrm{NMSE}(e_i) = \frac{1}{I_{g}^{*}{}_{\mathrm{m}} T} \sum_{n=1}^{T} e_i{}^2(n), \tag{35}$$

where $I_{g}^{*}{}_{\mathrm{m}}$ is the maximum value of the current command and $T$ is the sampling time.

## *5.1. Performance Verification in Steady-State*

Figures 6 and 7 show the experimental results of the grid-connected inverter system in steady-state. One can see from Figure 6 that the power factor (PF) values are more than 0.99 and the total harmonic distortion (THD) values of the current are less than 2% by the two control strategies. However, the THD and the NMSE values are reduced by 22.95% and 32.3% compared with the values of 1.83% and 0.0235 by GISMC in Figure 6a, and the values of 1.41% and 0.0159 by the proposed DRFNNISMC in Figure 6b, respectively. Moreover, the PF value is controlled to be 0.9925 by GISMC in Figure 6a, which is improved to 0.9985 by the proposed DRFNNISMC in Figure 6b.

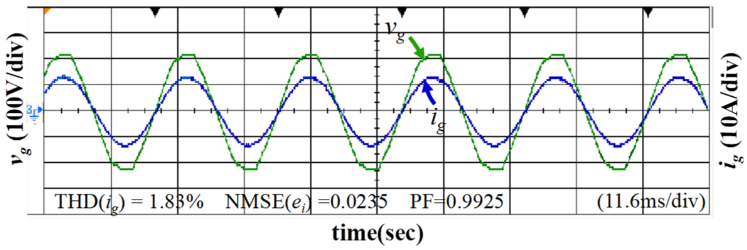


(**a**)

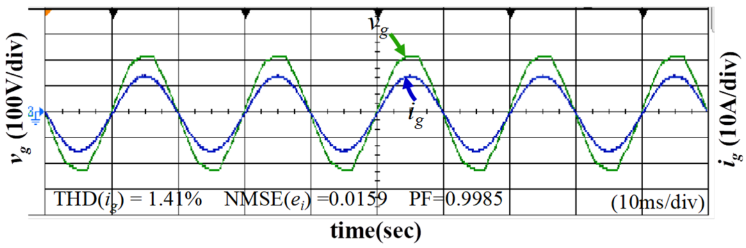


(**b**)

**Figure 6.** Experimental results of the grid-connected inverter in steady-state: (**a**) GISMC; (**b**) DRFNNISMC.

In addition, Figure 7 depicts the harmonic spectrum of the grid-connected current. The THD value is measured to be 1.83% and the third harmonic content is about 1.62% with the GISMC scheme in Figure 7a. Nevertheless, as seen in Figure 7b, the THD value is reduced to 1.41%, and the third harmonic content (0.67%) is reduced by more than one-half by the proposed DRFNNISMC scheme with the same filter inductance ($L_f$ = 2 mH). The proposed DRFNNISMC scheme can effectively improve the quality of the grid-connected current with a lower THD value, and fewer low order harmonics that are more difficult to eliminate. It can be seen in Figures 6 and 7 that superior quality and higher-precision tracking of the grid-connected current can be obtained by the proposed DRFNNISMC strategy in the steady-state.

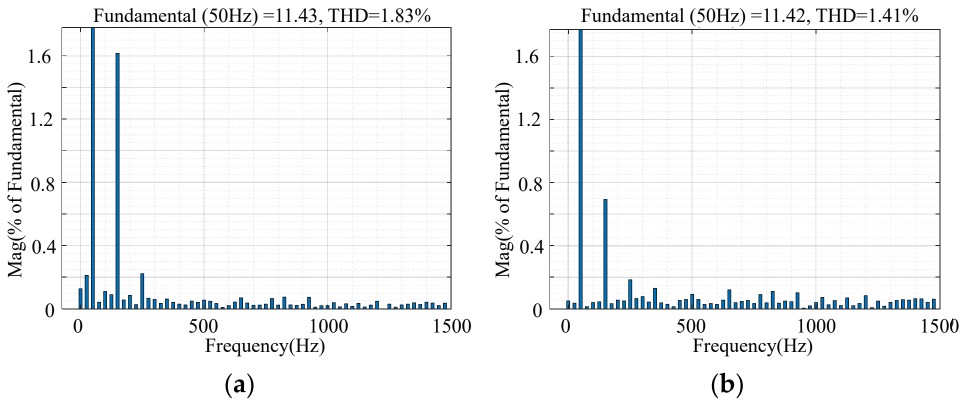


**Figure 7.** Harmonic spectrum of grid-connected current: (**a**) GISMC; (**b**) DRFNNISMC.

### 5.2. Verification of Dynamic Performance

Dynamic experimental research under the grid-connected power variations was performed to further validate the superior robustness of the proposed DRFNNISMC. The experimental voltage and current response under power variations from 1 kW to 0.5 kW and from 0.5 kW to 1 kW are demonstrated in Figures 8 and 9, respectively. As seen in Figures 8a and 9a, the chattering phenomenon occurs during the transition process against the power variations by the GISMC because of the large gain in the switching control term for coping with system uncertainties in (9); the NMSE values were recorded as 0.0312 and 0.0308 are reduced to 0.0195 and 0.0189, as shown in Figures 8b and 9b, which provides at least a 37.5% current tracking improvement from the proposed DRFNNISMC. Moreover, the transient oscillation is decreased effectively by the proposed DRFNNISMC with reasoning and online-learning capability and mathematical independence of the system. It can be concluded that the grid-connected inverter system controlled by the proposed DRFNNISMC framework possesses more robustness against power variation without oscillation, even though the power varies at the peak value.

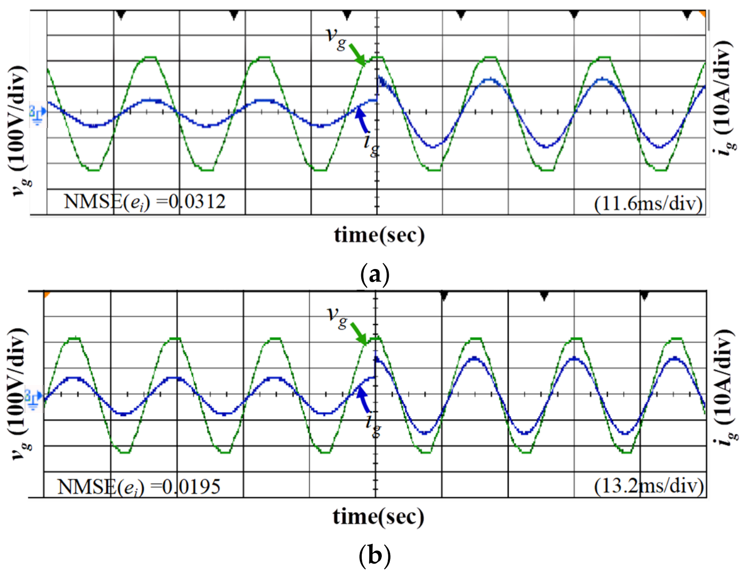


**Figure 8.** Experimental voltage and current response of grid-connected inverter under grid-connected power variations from 0.5 kW to 1 kW: (**a**) GISMC; (**b**) DRFNNISMC.

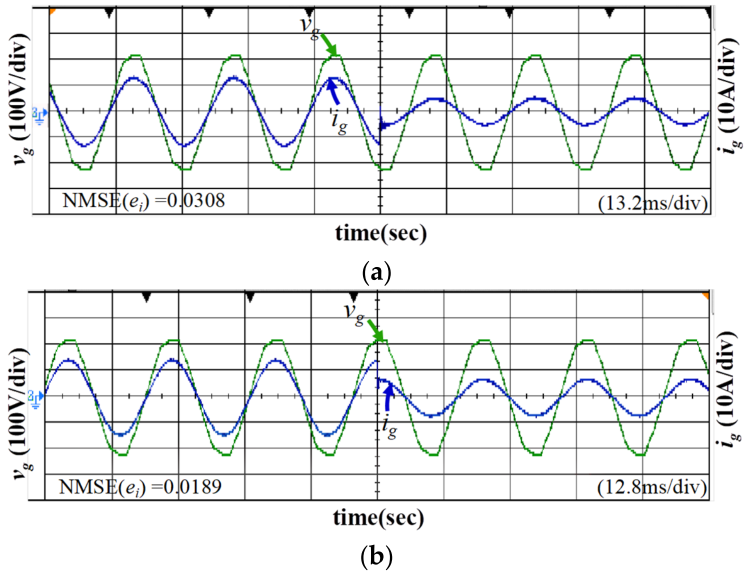


**Figure 9.** Experimental voltage and current response of grid-connected inverter under grid-connected power variations from 1 kW to 0.5 kW: (**a**) GISMC; (**b**) DRFNNISMC.

### *5.3. Robustness Property against Parameter Variations*

The fluctuation of DC-bus voltages due to distributed generations and filter inductance variation in the grid-connected inverter seems inevitable [33]. In order to illustrate the excellent robustness of the proposed DRFNNISMC against parameter variations, the experimental result of the grid-connected inverter with the DC-bus voltage deviation of 10% ($V_{dc}$ = 180 V) from the nominal voltage ($V_{dc}$ = 200 V) and the grid-connected inverter under the filter inductance with $L_f$ = 1.5 mH (with nominal filter inductance of $L_f$ = 2 mH) controlled by the proposed DRFNNISMC are depicted in Figures 10 and 11, respectively. Compared to Figure 6b, the THD value of the current and the NMSE values of the current tracking error are increased by 2.84% and 4.96%, and 2.51% and 3.77%, with the 10% voltage reduction and 25% inductance reduction, respectively. Moreover, the PF values are controlled to be more than 0.997 with a very slight decline. The experimental results of the grid-connected inverter shown in Figures 10 and 11 verify that the robust control performance of the proposed DRFNNISMC is less sensitive to parameter variations as a model-free framework.

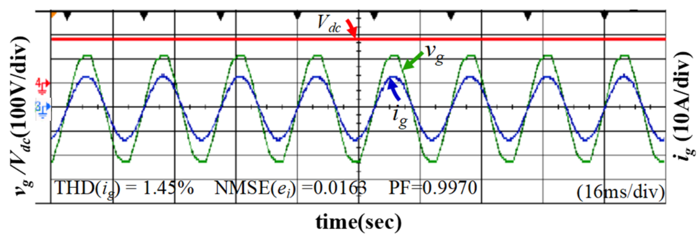


**Figure 10.** Experimental results of grid-connected inverter with DC-bus voltage ($V_{dc}$ = 180 V).

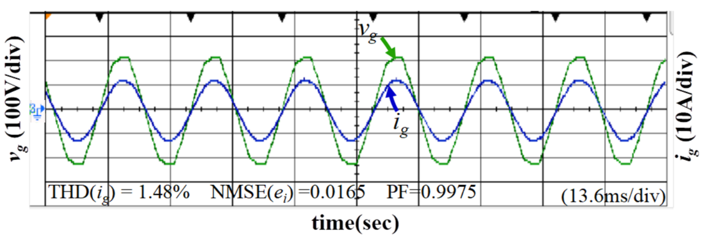


**Figure 11.** Experimental results of grid-connected inverter with inductance ($L_f$ = 1.5 mH).

### 5.4. Experimental Results Discussion

The experimental performance comparisons of the GISMC and the proposed DFNNISMC strategy are summarized in Table 2. The experimental comparisons with the GISMC strategy from Figures 6–9 show that the proposed DRFNNISMC possesses superior control performance with higher grid-connected power quality and higher-precision current tracking due to its capabilities of fuzzy reasoning and parameter online self-learning. Moreover, under the power variations, the proposed DRFNNISMC can provide at least 37.5% current tracking improvement and effectively decrease the chattering phenomenon in the GISMC system. In addition, the proposed DRFNNISMC as a model-free control scheme is less sensitive to parameter variations seen in Figures 10 and 11. Thus, the robustness of current tracking for the grid-connected inverter can be achieved by the proposed DRFNNISMC framework with the occurrence of system uncertainties without detailed system information.

**Table 2.** Experimental performance comparison of two control methods.

| Performance Control Methods | | GISMC | Proposed DRFNNISMC |
|---|---|---|---|
| Output power 1 kW | THD ($i_g$) | 1.83% | 1.41% |
| | PF | 0.9925 | 0.9985 |
| | NMSE ($e_i$) | 0.0235 | 0.0159 |
| Power variations from 0.5 kW to 1 kW | NMSE ($e_i$) | 0.0312 | 0.0195 |
| Power variations from 1 kW to 0.5 kW | NMSE ($e_i$) | 0.0308 | 0.0189 |
| DC-bus voltage fluctuation ($V_{dc}$ = 180 V) | THD ($i_g$) | / | 1.45% |
| | PF | / | 0.9970 |
| | NMSE ($e_i$) | / | 0.0163 |
| Inductance variation ($L_f$ = 1.5 mH) | THD ($i_g$) | / | 1.48% |
| | PF | / | 0.0165 |
| | NMSE ($e_i$) | / | 0.9975 |
| Dependence on system parameters | | High | None |
| Robustness | | Good | Favorable |
| Chattering | | Chattering | None |
| Learning ability | | None | Online self-learning |

## 6. Conclusions

A dynamic recurrent fuzzy-neural-network imitating sliding-mode control (DRFNNISMC) framework is proposed in this study to construct an excellent performance control system for an inverter system in grid-connected mode. Due to its ability to approximate continuous functions, the designed DRFNN works as a major controller to approximate the GISMC law without the extra compensator. The concept of a Petri net with the simplified rule firing mechanism is introduced to lessen the computational load of parameter learning. Moreover, the frame of internal recurrent loops is utilized to improve the dynamic capability of network mapping. In addition, the adaptation laws are derived by the Lyapunov stability theory and the projection theorem to assure the convergence of the network parameters and the stability of the proposed DRFNNISMC system.

In order to further enhance the robustness against system uncertainties, type-2 fuzzy neural networks can be developed to approximate the nonlinear control laws. Moreover, the intelligent controller for the grid-connected inverter can designed and analyzed by considering the influence of weak grid characteristics in order to improve the grid-connected power quality of the microgrid (MG). In addition, multi-function grid-connected inverters with the compound functions of grid-connected power generation as well as power quality management (e.g., voltage sags, harmonic currents, and reactive currents compensation) can be further investigated to promote the customization of MG systems in future work.

**Author Contributions:** Mathematical modeling, methodology, Y.W., Y.Y. and R.L.; hardware, Y.Y. and T.G.; software, T.G. and W.Z.; validation, T.G. and W.Z.; writing—original draft preparation, Y.Y.; writing—review and editing Y.W., Y.Y. and R.L. All authors have read and agreed to the published version of the manuscript.

**Funding:** This research was funded by the Natural Science Research Project of Huaian under Grant No. HAB201905; Huai'an key laboratory of motion control and converter technology under Grant No. HAP201903; Science and technology project of Jiangsu Provincial Department of housing and urban rural development under Grant No. 2019ZD0062; Natural Science Research Project of Huaian under Grant No. HAB202062.

**Institutional Review Board Statement:** Not applicable.

**Informed Consent Statement:** Not applicable.

**Data Availability Statement:** Not applicable.

**Conflicts of Interest:** The authors declare no conflict of interest.

## Abbreviations

| | |
|---|---|
| MG | Microgrid |
| UG | Utility grid |
| SMC | Sliding-mode control |
| GSMC | Global sliding mode control |
| GISMC | Global integral sliding-mode control |
| FNN | Fuzzy neural network |
| PN | Petri net |
| RFNN | Recurrent fuzzy neural network |
| DRFNN | Dynamic recurrent fuzzy-neural-network |
| DRFNNISMC | Dynamic recurrent fuzzy-neural-network imitating sliding-mode control |
| DC | Direct current |
| AC | Alternating current |
| KVL | Kirchhoff voltage law |
| PLL | Phase-locked loop |
| DSP | Digital signal processor |
| PWM | Pulse width modulation |
| NMSE | Normalized mean square error |
| PF | Power factor |
| THD | Total harmonic distortion |
| Variables and parameters | |
| $L_f$ | Filter inductor |
| $R_{Lf}$ | Equivalent resistors of filter |
| $V_{dc}$ | DC bus input voltage of inverter |
| $v_{AB}$ | AC output voltage of inverter |
| $i_g$ | Grid-connected current |
| $v_g$ | Voltage of utility grid |
| $v_{ld}$ | Disturbance in utility grid |
| $K_c$ | PWM gain of inverter |
| $v_t$ | Amplitude of triangular-carrier signal |
| $v_u$ | Modulation signal |
| X | System state |
| $u$ | Control input |
| $f, g$ | Variable of state equation |
| $b_{pn}, d_{pn}$ | Criterion values of state equation coefficients |
| $b_p, d_p$ | State equation coefficients |
| $\Delta b_{pn}, \Delta d_{pn}$ | Difference between real and criterion values of state equation coefficients |

| | |
|---|---|
| $\boldsymbol{\varphi}(t)$ | System lumped uncertainty |
| $\rho$ | Boundary value of system lumped uncertainty |
| $i_g^*$ | Reference signal of grid-connected current |
| $u_b$ | Baseline model control law |
| $e_i, e_{i0}$ | Current tracking error, initial value of error |
| S | global integral sliding-surface |
| $K_i, K_s$ | Controller parameters of GISMC |
| $u_1$ | Control law of GISMC |
| $V_1$ | First Lyapunov function candidate for GISMC scheme |
| $q_i\|_{i=1,\cdots,n}$ | Input variables of DRFNN |
| $\boldsymbol{\gamma} = [\gamma_1^1 \cdots \gamma_1^{N_{p1}} \cdots \gamma_n^1 \cdots \gamma_n^{N_{pn}}]^T\Big\|_{i=1,\cdots,n}$ | Recurrent weight vector in membership layer |
| $\boldsymbol{c} = [c_1^1 \cdots c_1^{N_{p1}} \cdots c_n^1 \cdots c_n^{N_{pn}}]^T\Big\|_{i=1,\cdots,n}$ | Mean deviation vector of Gaussian functions |
| $\boldsymbol{b} = [b_1^1 \cdots b_1^{N_{p1}} \cdots b_n^1 \cdots b_n^{N_{pn}}]^T\Big\|_{i=1,\cdots,n}$ | Standard deviation vector of Gaussian functions |
| $f_i^j$ | Input of *j*th membership neuron for the *i*th input signal |
| $\mu_i^j$ | Output of *j*th membership neuron for the *i*th input signal |
| $N_{pi}$ | Number of nodes in membership layer for *i*th input |
| $N_r$ | Total number of membership functions of all input signals |
| $p_i^j$ | Transition of *j*th membership neuron for the *i*th input signal |
| $d_{\text{th}}$ | Dynamic threshold value |
| $\alpha_f, \beta_f$ | Parameters of dynamic threshold |
| $\boldsymbol{l} = [l_1, \cdots, l_{N_l}] \in R^{N_l \times 1}$ | Output of rule layer |
| $N_l$ | Number of nodes in rule layer |
| $\boldsymbol{W} = [w_1 \cdots w_h \cdots w_{N_l}]$ | Connecting weight vector from rule layer to output layer |
| y | Output of DRFNN |
| $\boldsymbol{W}^*, \boldsymbol{c}^*, \boldsymbol{b}^*, \gamma^*, \boldsymbol{l}^*$ | Optimal vectors of $\boldsymbol{W}, \boldsymbol{c}, \boldsymbol{b}, \boldsymbol{\gamma}, \boldsymbol{l}$ |
| $\hat{\boldsymbol{W}}, \hat{\boldsymbol{c}}, \hat{\boldsymbol{b}}, \hat{\boldsymbol{\gamma}}, \hat{\boldsymbol{l}}$ | Estimated vectors of $\boldsymbol{W}^*, \boldsymbol{c}^*, \boldsymbol{b}^*, \gamma^*, \boldsymbol{l}^*$ |
| $\widetilde{\boldsymbol{W}}, \widetilde{\boldsymbol{c}}, \widetilde{\boldsymbol{b}}, \widetilde{\boldsymbol{\gamma}}, \widetilde{\boldsymbol{l}}$ | Difference between optimal and estimated vector |
| $u_2^*$ | Optimal DRNNISMC law |
| $\varepsilon$ | Minimum mapping error vector |
| $\hat{u}_2$ | Estimation of $u_2^*$ |
| $\widetilde{u}$ | Approximation error |
| $\boldsymbol{l}_c, \boldsymbol{l}_b, \boldsymbol{l}_\gamma$ | Coefficient vectors of first-order terms in Taylor series |
| $\boldsymbol{h}$ | Summation of higher-order term in Taylor series |
| $H$ | Uncertain term in approximation error |
| $\boldsymbol{b}= [b_w\ b_c\ b_b\ b_\gamma]$ | Bound vectors of $\boldsymbol{W}, \boldsymbol{c}, \boldsymbol{b}, \boldsymbol{\gamma}$ |
| $\boldsymbol{\eta}= [\eta_w\ \eta_c\ \eta_b\ \eta_\gamma]$ | Learning rates of $\boldsymbol{W}, \boldsymbol{c}, \boldsymbol{b}, \boldsymbol{\gamma}$ |
| $V_2$ | Second Lyapunov function candidate for DRFNNISMC scheme |
| $G$ | Defined function for proof of stability and convergence of DRFNNISMC system |

## Appendix A

The derivative of Equation (31) with respect to time can be expressed as

$$\dot{V}_2(s, \widetilde{\boldsymbol{W}}, \widetilde{\boldsymbol{c}}, \widetilde{\boldsymbol{b}}, \widetilde{\boldsymbol{\gamma}}) = s\dot{s} - \frac{\widetilde{\boldsymbol{W}}\dot{\hat{\boldsymbol{W}}}^T}{\eta_w} - \frac{\dot{\hat{\boldsymbol{c}}}^T\widetilde{\boldsymbol{c}}}{\eta_c} - \frac{\dot{\hat{\boldsymbol{b}}}^T\widetilde{\boldsymbol{b}}}{\eta_b} - \frac{\dot{\hat{\boldsymbol{\gamma}}}^T\widetilde{\boldsymbol{\gamma}}}{\eta_\gamma}, \tag{A1}$$

replacing $u_1$ and $\widetilde{u}$ with Equations (9) and (23), respectively. The actual DRNNISMC law as shown in Equation (19) can be rewritten as

$$\begin{aligned} \hat{u}_2 &= u_1 - \widetilde{u} \\ &= b_{pn}^{-1}[-d_{pn}f(t) + \dot{x}^* + K_i e_i + K_s \text{sgn}(s)] \ , \\ &\quad -(\widetilde{\boldsymbol{W}}\hat{\boldsymbol{l}} + \hat{\boldsymbol{W}}\boldsymbol{l}_c\widetilde{\boldsymbol{c}} + \hat{\boldsymbol{W}}\boldsymbol{l}_b\widetilde{\boldsymbol{b}} + \hat{\boldsymbol{W}}\boldsymbol{l}_\gamma\widetilde{\boldsymbol{\gamma}} + H) \end{aligned} \tag{A2}$$

Based on the actual DRNNISMC law, the derivative of the global integral sliding-surface ($s$) with respect to time can be re-expressed as

$$\dot{s} = -K_S \mathrm{sgn}(s) - \psi + \left(\widetilde{\boldsymbol{W}}\hat{\boldsymbol{l}} + \hat{\boldsymbol{W}}\boldsymbol{l}_c\widetilde{\boldsymbol{c}} + \hat{\boldsymbol{W}}\boldsymbol{l}_b\widetilde{\boldsymbol{b}} + \hat{\boldsymbol{W}}\boldsymbol{l}_\gamma\widetilde{\gamma} + H\right), \tag{A3}$$

By substituting (A2) into (A1), one can obtain

$$\begin{aligned}
\dot{V}_2(s, \widetilde{\boldsymbol{W}}, \widetilde{\boldsymbol{c}}, \widetilde{\boldsymbol{b}}, \widetilde{\gamma}) &= s[-K_S \mathrm{sgn}(s) - \psi] + s\left(\widetilde{\boldsymbol{W}}\hat{\boldsymbol{l}} + \hat{\boldsymbol{W}}\boldsymbol{l}_c\widetilde{\boldsymbol{c}} + \hat{\boldsymbol{W}}\boldsymbol{l}_b\widetilde{\boldsymbol{b}} + \hat{\boldsymbol{W}}\boldsymbol{l}_\gamma\widetilde{\gamma} + H)\right] \\
&\quad - \frac{\widetilde{\boldsymbol{W}}\dot{\hat{\boldsymbol{W}}}^T}{\eta_w} - \frac{\dot{\hat{\boldsymbol{c}}}^T\widetilde{\boldsymbol{c}}}{\eta_c} - \frac{\dot{\hat{\boldsymbol{b}}}^T\widetilde{\boldsymbol{b}}}{\eta_b} - \frac{\dot{\hat{\gamma}}^T\widetilde{\gamma}}{\eta_\gamma} \\
&= s[-K_S \mathrm{sgn}(s) - \psi + H] + \left(s\widetilde{\boldsymbol{W}}\hat{\boldsymbol{l}} - \frac{\widetilde{\boldsymbol{W}}\dot{\hat{\boldsymbol{W}}}^T}{\eta_w}\right) + \left(s\hat{\boldsymbol{W}}\boldsymbol{l}_c\widetilde{\boldsymbol{c}} - -\frac{\dot{\hat{\boldsymbol{c}}}^T\widetilde{\boldsymbol{c}}}{\eta_c}\right) \\
&\quad + \left(s\hat{\boldsymbol{W}}\boldsymbol{l}_b\widetilde{\boldsymbol{b}} - \frac{\dot{\hat{\boldsymbol{b}}}^T\widetilde{\boldsymbol{b}}}{\eta_b}\right) + \left(s\hat{\boldsymbol{W}}\boldsymbol{l}_\gamma\widetilde{\gamma} - \frac{\dot{\hat{\gamma}}^T\widetilde{\gamma}}{\eta_\gamma}\right) \\
&= s[-K_S \mathrm{sgn}(s) - \psi + H] + V_w + V_c + V_b + V_\gamma
\end{aligned}, \tag{A4}$$

where $V_w = s\widetilde{\boldsymbol{W}}\hat{\boldsymbol{l}} - \frac{\widetilde{\boldsymbol{W}}\dot{\hat{\boldsymbol{W}}}^T}{\eta_w}$, $V_c = s\hat{\boldsymbol{W}}\boldsymbol{l}_c\widetilde{\boldsymbol{c}} - \frac{\dot{\hat{\boldsymbol{c}}}^T\widetilde{\boldsymbol{c}}}{\eta_c}$, $V_b = s\hat{\boldsymbol{W}}\boldsymbol{l}_b\widetilde{\boldsymbol{b}} - \frac{\dot{\hat{\boldsymbol{b}}}^T\widetilde{\boldsymbol{b}}}{\eta_b}$, $V_\gamma = s\hat{\boldsymbol{W}}\boldsymbol{l}_\gamma\widetilde{\gamma} - \frac{\dot{\hat{\gamma}}^T\widetilde{\gamma}}{\eta_\gamma}$.

$V_w$ can be rewritten as the following expression according to the adaptation law of the output weights designed as shown in Equation (24).

By Equation (24),

$$V_w = s\widetilde{\boldsymbol{W}}\hat{\boldsymbol{l}} - \frac{\widetilde{\boldsymbol{W}}\dot{\hat{\boldsymbol{W}}}^T}{\eta_w} = s\widetilde{\boldsymbol{W}}\hat{\boldsymbol{l}} - \frac{\widetilde{\boldsymbol{W}}(\eta_w s\hat{\boldsymbol{l}})}{\eta_w} = 0, \tag{A5}$$

By Equation (25),

$$V_w = s\widetilde{\boldsymbol{W}}\hat{\boldsymbol{l}} - \frac{\widetilde{\boldsymbol{W}}\dot{\hat{\boldsymbol{W}}}^T}{\eta_w} = \frac{\widetilde{\boldsymbol{W}}s\hat{\boldsymbol{l}}\hat{\boldsymbol{W}}\hat{\boldsymbol{W}}^T}{\|\hat{\boldsymbol{W}}\|^2} = \frac{s\hat{\boldsymbol{W}}\hat{\boldsymbol{l}}}{\|\hat{\boldsymbol{W}}\|^2}\widetilde{\boldsymbol{W}}\hat{\boldsymbol{W}}^T, \tag{A6}$$

The result of $\widetilde{\boldsymbol{W}}\hat{\boldsymbol{W}}^T = (\boldsymbol{W}^* - \hat{\boldsymbol{W}})\hat{\boldsymbol{W}}^T = \frac{1}{2}(\|\boldsymbol{W}^*\|^2 - \|\hat{\boldsymbol{W}}\|^2 - \|\widetilde{\boldsymbol{W}}\|^2) < 0$ is satisfied according to the conditions of $\|\hat{\boldsymbol{W}}\| = b_w$ and $s\hat{\boldsymbol{W}}\hat{\boldsymbol{l}} > 0$, and the result of $V_w < 0$ can be guaranteed due to $\|\boldsymbol{W}^*\| < b_w = \|\hat{\boldsymbol{W}}\|$.

According to the analysis of Equations (A5) and (A6), one find that $V_w \leq 0$. Similarly, the results of $V_c \leq 0$, $V_b \leq 0$, and $V_\gamma \leq 0$ can also be satisfied. Then, (A4) can be re-expressed as

$$\begin{aligned}
\dot{V}_2(s, \widetilde{\boldsymbol{W}}, \widetilde{\boldsymbol{c}}, \widetilde{\boldsymbol{b}}, \widetilde{\gamma}) &= s[-K_S \mathrm{sgn}(s) - \psi + H] + V_w + V_c + V_b + V_\gamma \\
&\leq sK_S \mathrm{sgn} + s(H - \psi) \\
&\leq -(K_S - |H - \psi|)|s| \leq 0
\end{aligned}, \tag{A7}$$

If the controller gain of $K_S > |H - \psi|$ is satisfied, the result of $\dot{V}_2(s, \widetilde{\boldsymbol{W}}, \widetilde{\boldsymbol{c}}, \widetilde{\boldsymbol{b}}, \widetilde{\gamma}) \leq 0$ can be obtained.

## References


1. Muhtadi, A.; Pandit, D.; Nguyen, N.; Mitra, J. Distributed Energy Resources Based Microgrid: Review of Architecture, Control, and Reliability. *IEEE Trans. Ind. Appl.* **2021**, *57*, 2223–2235. [CrossRef]
2. Bihari, S.P.; Sadhu, P.K.; Sarita, K.; Khan, B.; Arya, L.D.; Saket, R.K.; Kothari, D.P. A Comprehensive Review of Microgrid Control Mechanism and Impact Assessment for Hybrid Renewable Energy Integration. *IEEE Access* **2021**, *9*, 88942–88958. [CrossRef]
3. Wu, D.; Tang, F.; Dragicevic, T.; Vasquez, J.C.; Guerrero, J.M. A control architecture to coordinate renewable energy sources and energy storage systems in islanded microgrids. *IEEE Trans. Smart Grid* **2015**, *6*, 1156–1166. [CrossRef]
4. Kakran, S.; Chanana, S. Smart operations of smart grids integrated with distributed generation: A review. *Renew. Sustain. Energy Rev.* **2018**, *81*, 524–535. [CrossRef]

5. Chen, X.; Ruan, X.; Yang, D.; Zhao, W.; Jia, L. Injected grid current quality improvement for a voltage-controlled grid-connected inverter. *IEEE Trans. Power Electron.* **2017**, *33*, 1247–1258. [CrossRef]
6. Kumar, N.; Saha, T.K.; Dey, J. Sliding-mode control of PWM dual inverter-based grid-connected PV system: Modeling and performance analysis. *IEEE J. Emerg. Sel. Top. Power Electron.* **2016**, *4*, 435–444. [CrossRef]
7. Dhar, S.; Dash, P.K. A new backstepping finite time sliding mode control of grid connected PV system using multivariable dynamic VSC model. *Int. J. Electr. Power Energy Syst.* **2016**, *82*, 314–330. [CrossRef]
8. Alquthami, T.; Zulfiqar, M.; Kamran, M.; Milyani, A.H.; Rasheed, M.B. A Performance Comparison of Machine Learning Algorithms for Load Forecasting in Smart Grid. *IEEE Access* **2022**, *10*, 48419–48433. [CrossRef]
9. Xiao, D.L.; Chen, H.Y.; Wei, C.; Bai, X.Q. Statistical Measure for Risk-Seeking Stochastic Wind Power Offering Strategies in Electricity Markets. *J. Mod. Power Syst. Clean Energy* **2021**, 1–6. [CrossRef]
10. Zeb, K.; Nazir, M.; Ahmad, I.; Uddin, W.; Kim, H.-J. Control of Transformerless Inverter-Based Two-Stage Grid-Connected Photovoltaic System Using Adaptive-PI and Adaptive Sliding Mode Controllers. *Energies* **2021**, *14*, 2546. [CrossRef]
11. Chen, S.; Lai, Y.M.; Tan, S.C.; Tse, C.K. Fast response low harmonic distortion control scheme for voltage source inverters. *IET Power Electron.* **2009**, *2*, 574–584. [CrossRef]
12. Chu, Y.; Fei, J.; Hou, S. Dynamic Global Proportional Integral Derivative Sliding Mode Control Using Radial Basis Function Neural Compensator for Three-Phase Active Power Filter. *Trans. Inst. Meas. Control* **2018**, *40*, 3549–3559. [CrossRef]
13. Wai, R.J.; Lin, C.Y.; Huang, Y.C.; Chang, Y.R. Design of high-performance stand-alone and grid-connected inverter for distributed generation applications. *IEEE Trans. Ind. Electron.* **2013**, *60*, 1542–1555. [CrossRef]
14. Wang, H.; Li, Z.; Jin, X.; Huang, Y.; Kong, H.; Yu, M.; Ping, Z.; Sun, Z. Adaptive Integral Terminal Sliding Mode Control for Automobile Electronic Throttle via an Uncertainty Observer and Experimental Validation. *IEEE Trans. Veh. Technol.* **2018**, *67*, 8129–8143. [CrossRef]
15. Shi, P.; Liu, M.; Zhang, L. Fault-Tolerant Sliding-Mode-Observer Synthesis of Markovian Jump Systems Using Quantized Measurements. *IEEE Trans. Ind. Electron.* **2015**, *62*, 5910–5918. [CrossRef]
16. Shadoul, M.; Yousef, H.; Abri, R.; Al-Hinai, A. Adaptive Fuzzy Approximation Control of PV Grid-Connected Inverters. *Energies* **2021**, *14*, 942. [CrossRef]
17. Livinti, P. Comparative Study of a Photovoltaic System Connected to a Three-Phase Grid by Using PI or Fuzzy Logic Controllers. *Sustainability* **2021**, *13*, 2562. [CrossRef]
18. Haq, I.U.; Khan, Q.; Khan, I.; Akmeliawati, R.; Nisar, K.S.; Khan, I. Maximum power extraction strategy for variable speed wind turbine system via neuro-adaptive generalized global sliding mode controller. *IEEE Access* **2020**, *8*, 128536–128547. [CrossRef]
19. Zhu, Y.; Fei, J. Adaptive Global Fast Terminal Sliding Mode Control of Grid-connected Photovoltaic System Using Fuzzy Neural Network Approach. *IEEE Access* **2017**, *5*, 9476–9484. [CrossRef]
20. Chu, Y.; Fei, J.; Hou, S. Adaptive global sliding-mode control for dynamic systems using double hidden layer recurrent neural network structure. *IEEE Trans Neural Netw. Learn. Syst.* **2020**, *31*, 1297–1309. [CrossRef]
21. Wai, R.; Lin, Y.; Liu, Y. Design of Adaptive Fuzzy-Neural-Network Control for a Single-Stage Boost Inverter. *IEEE Trans. Power Electron.* **2015**, *30*, 7282–7298. [CrossRef]
22. Yang, Y.; Wai, R.J. Design of adaptive fuzzy-neural-network-imitating sliding-mode control for parallel-inverter system in islanded micro-grid. *IEEE Access* **2021**, *9*, 56376–56396. [CrossRef]
23. Wai, R.J.; Muthusamy, R. Design of Fuzzy-Neural-Network-Inherited Backstepping Control for Robot Manipulator Including Actuator Dynamics. *IEEE Trans. Fuzzy Syst.* **2014**, *22*, 709–722. [CrossRef]
24. Wai, R.; Yao, J.; Lee, J. Backstepping Fuzzy-Neural-Network Control Design for Hybrid Maglev Transportation System. *IEEE Trans. Neural Netw. Learn. Syst.* **2015**, *26*, 302–317.
25. Wai, R.J.; Liu, C.M. Design of Dynamic Petri Recurrent Fuzzy Neural Network and Its Application to Path-Tracking Control of Nonholonomic Mobile Robot. *IEEE Trans. Ind. Electron.* **2009**, *56*, 2667–2683.
26. El-Sousy, F.F.M.; Abuhasel, K.A. Adaptive Nonlinear Disturbance Observer Using a Double-Loop Self-Organizing Recurrent Wavelet Neural Network for a Two-Axis Motion Control System. *IEEE Trans. Ind. Appl.* **2018**, *54*, 764–786. [CrossRef]
27. Liu, S.; Guo, X.; Zhang, L. Robust Adaptive Backstepping Sliding Mode Control for Six-Phase Permanent Magnet Synchronous Motor Using Recurrent Wavelet Fuzzy Neural Network. *IEEE Access* **2017**, *5*, 14502–14515.
28. Chen, F.; Fei, J.; Xue, Y. Double Recurrent Perturbation Fuzzy Neural Network Fractional-Order Sliding Mode Control of Micro Gyroscope. *IEEE Access* **2021**, *9*, 55352–55363. [CrossRef]
29. Fei, J.; Liu, L. Real-Time Nonlinear Model Predictive Control of Active Power Filter Using Self-Feedback Recurrent Fuzzy Neural Network Estimator. *IEEE Trans. Ind. Electron.* **2022**, *69*, 8366–8376. [CrossRef]
30. Tan, K.H.; Tseng, T.Y. Seamless Switching and Grid Reconnection of Microgrid Using Petri Recurrent Wavelet Fuzzy Neural Network. *IEEE Trans. Power Electron.* **2021**, *36*, 11847–11861. [CrossRef]
31. Lin, F.J.; Chen, S.G.; Hsu, C.W. Intelligent backstepping control using recurrent feature selection fuzzy neural network for synchronous reluctance motor position servo drive system. *IEEE Trans. Fuzzy Syst.* **2019**, *27*, 413–427. [CrossRef]
32. Hou, S.; Chu, Y.; Fei, J. Intelligent global sliding mode control using recurrent feature selection neural network for active power filter. *IEEE Trans. Ind. Electron.* **2021**, *68*, 7320–7329. [CrossRef]

33. Li, Y.; Mai, R.; Lu, L.; He, Z. Active and reactive currents decomposition-based control of angle and magnitude of current for a parallel multi-inverter IPT system. *IEEE Trans. Power Electron.* **2017**, *32*, 1602–1614. [CrossRef]
34. Astrom, K.J.; Wittenmark, B. *Adaptive Control*; Addison-Wesley: New York, NY, USA, 1995.
35. Wang, L.X. *A Course in Fuzzy Systems and Control*; Prentice-Hall: Englewood Cliffs, NJ, USA, 1997.